scientific reports

Check for updates

OPEN

Dual-band millimetre wave MIMO antenna with reduced mutual coupling based on optimized parasitic structure and ground modification

Bashar A. F. Esmail[1], Dustin Isleifson[1] & Slawomir Koziel[2,3]✉

In this study, a high-isolation dual-band (28/38 GHz) multiple-input–multiple-output (MIMO) antenna for 5G millimeter-wave indoor applications is presented. The antenna consists of two interconnected patches. The primary patch is connected to the inset feed, while the secondary patch is arc-shaped and positioned over the main patch, opposite to the feed. Both patches function in the lower 28 GHz band, while the primary patch is accountable for inducing the upper 38 GHz band. An expedited trust-region (TR) algorithm is employed to optimize the dimensions of the antenna components, ensuring the antenna operates efficiently with high reflection at both bands. The antenna demonstrates a gain exceeding 7 dBi at both frequencies. An array of four antennas is configured orthogonally to create a MIMO system with isolation surpassing 19 dB. The isolation is further enhanced through the addition of a circular parasitic patch at the front and modifications made to the ground. The TR method is employed again to optimize their parameters and achieve the desired isolation, exceeding 32 dB at both bands. The MIMO system demonstrates outstanding diversity performance at both frequencies, characterized by low values of the envelope correlation coefficient (ECC) (< 10 – 4), channel capacity loss (CCL) (< 0.03 bit/s/Hz), and total active reflection coefficient (TARC) (< – 10 dB). Additionally, it secures a diversity gain (DG) exceeding 9.99 dB. The MIMO system is manufactured and tested, showing good alignment between simulation and measurement data for all performance metrics.

Keywords Dual band antenna, Millimeter-wave, MIMO, Design optimization, Trust-region methods

Advancements in wireless communications over the past decade have been notable, especially in terms of broadened bandwidth and higher data rates. To meet these requirements by the communication hardware, fifth-generation (5G) technology has been deployed. Implementing 5G systems is proposed through the utilization of the millimeter-wave band, with allocated frequency bands for mobile networks at 28, 38, 60, and 73 GHz[1–3]. Many literature reports delve into the frequencies of 28 and 38 GHz, highlighting their satisfactory bandwidth and lower path losses in comparison to higher millimeter-wave frequencies[4–6]. Multiband antennas hold appeal for 5G systems as they enable the system to remain compact in terms of physical size. Addressing the challenge of enhancing transmission quality in the millimeter-wave spectrum involves leveraging additional technologies, with recognized as a key component for 5G communication systems[7]. Multi-band antennas offer an attractive solution for 5G systems, as a single radiating element can cover multiple frequencies. Various technologies have been proposed to achieve dual-band properties, including the substrate-integrated waveguide (SIW)[8–10]. In[9], the antenna features a circular-shaped cavity resonator using the SIW technique and a square-ring slot, designed to operate at two nearby frequencies, around 5.8 and 5.9 GHz, with low cross-polarization over the full operating bandwidth. Additionally, the authors of[10] introduced a low-profile, cavity-backed, dual-band, dual-polarized antenna operating at 5.2 GHz and 5.8 GHz. This antenna consists of two planar SIW cavities, each with diamond-ring shaped slots etched in them for radiation. The design provides linear polarization at

[1]Department of Electrical & Computer Engineering, University of Manitoba, Winnipeg, MB R3T 5V6, Canada. [2]Department of Engineering, Reykjavik University, 102 Reykjavík, Iceland. [3]Faculty of Electronics, Telecommunications and Informatics, Gdansk University of Technology, 80-233 Gdansk, Poland. ✉email: koziel@ru.is

the lower frequency band and circular polarization at the higher frequency band. On the other hand, MIMO contributes to improved channel capacity, enhanced spectrum efficiency, and diminished multipath effects[11,12]. Nevertheless, a strong coupling between radiating elements presents a significant challenge for MIMO antenna systems, particularly when operating within the confines of limited antenna deployment space. This coupling can cause interference among near-situated radiating antennas, resulting in signal quality degradation, amplified interference, and decreased channel capacity. As communication systems advance rapidly, there is an increasing need for millimeter-wave multiband and high-isolation MIMO antennas to fulfill the requirements of 5G systems. Numerous MIMO antennas in the millimeter-wave range have been introduced in literature[13–18]. No mutual coupling reduction methods were utilized in these studies, relying instead on the effective arrangement of the radiating elements to achieve good isolation. In[13], a two-port MIMO system operating at 27 and 39 GHz was introduced. Isolation better than 25 dB is achieved with a low-profile structure. A four-port MIMO antenna has been detailed in[14]. The system operates at 27.1 and 48.7 GHz, achieving high isolation of better than 27 dB at both frequencies. In[15], the authors described a two-port MIMO-based patch antenna designed for operation at 28 and 38 GHz. The design provides isolation exceeding 20 dB and achieves around 5 dBi gain across the two operational bands. In[16], two monopole antennas are arranged orthogonally to construct a MIMO system operating at 28/38 GHz. The design achieves mutual coupling of less than −20 dB with very low gain, measuring 1.27 dB 1.83 dB at 28 GHz and 38 GHz, respectively. However, these devices exhibit bulky structures, and there is a need for further enhancement of isolation to construct a robust millimeter-wave system. In[18], quad-port MIMO antennas with hexagonal patch shapes were proposed, achieving 25 dB isolation at 35 GHz. Meanwhile, in[19], quad-port MIMO antennas with infinity patch shapes were proposed, achieving 29 dB isolation at 28 GHz. On the other hand, the literature presents diverse decoupling techniques, including embedding parasitic elements and utilizing artificial materials. The incorporation of artificial materials with extraordinary features, such as electromagnetic band-gap (EBG), metasurface, and metamaterials, has been implemented as decoupling structures, positioned either between or above the radiating elements[20–25]. The authors of[21] and[21] proposed a two-port MIMO system that integrates metamaterials between the radiating elements and implements a ground modification to enhance isolation at 28 and 38 GHz. These systems ensure significant isolation with a low-profile configuration. In[22] and[23], EBG unit cells were integrated with two-port MIMO systems, resulting in a high isolation of 24 dB and 37 dB, respectively. Sehrai et al.[24] proposed incorporating a metasurface layer above a Quad-port MIMO to reduce the mutual coupling to less than −20 dB at 26 GHz.

Incorporating parasitic elements, either on the patch or the ground, has proven to be effective in reducing mutual coupling[26–30]. In[26], the authors introduced a C-shaped structure between the two monopole antennas. This addition was engineered to enhance isolation, elevated to 23 dB at a frequency of 28 GHz. In[27], a MIMO system is constructed using two-port dielectric resonator antennas (DRA) operating at 28 GHz. Metal strips are printed on the upper adjacent surfaces of these antennas to enhance isolation between the two elements, achieving an improvement of 24 dB. The authors of[28] presented a dual-element MIMO antenna engineered to attain high isolation, measuring 32 dB at 16 GHz. In the research reported in[29], a two-port MIMO system based on a slotted circular patch antenna was constructed, demonstrating isolation levels exceeding 32 dB at 28 GHz. A parasitic patch was strategically placed between the two MIMO elements to improve isolation. This parasitic element takes the form of a C-shape and is incorporated around the two radiating elements. In[30], a compact four-element MIMO antenna with decoupling lines is proposed for 5G millimeter-wave applications. Two cross lines are incorporated between the tilted spade-shaped radiators to enhance isolation, achieving better than 30 dB across the operating range of 23.9–40.1 GHz. Gain values measured are between 3 and 5 dB, with radiation efficiencies ranging from 65 to 85% throughout the entire bandwidth. Enhancing isolation and increasing the number of MIMO elements could have a significant impact on improving the performance of wireless communications at the millimeter-wave band.

This paper introduces a four-port MIMO system tailored for operation at both 28 and 38 GHz, characterized by a low profile, minimized mutual coupling, and high gain. The antenna configuration involves a patch antenna of two parts, enabling the achievement of dual-band properties. The primary component, linked to the feed, is coupled with an arc-shaped parasitic patch to resonate at the first 28 GHz band. The second band, which operates at 38 GHz, is acquired through the main patch. All relevant antenna parameters were simultaneously optimized utilizing a trust-region algorithm to enhance reflection while maintaining a gain of over 7 dBi across both frequency bands. By employing numerical optimization, the process of adjusting the antenna's dimensions can be streamlined, reducing the time needed. Since the antenna's performance often depends on precise dimension adjustments and accurate formulas are not always available for all antenna configurations, implementing optimization techniques becomes the most effective strategy for achieving the desired results with minimal time and effort. In this study, the trust-region optimization method was used to determine the optimal antenna dimensions and achieve the desired outcomes. Subsequently, a quad-port MIMO system was constructed and thoroughly analyzed. To further improve performance, a parasitic patch was introduced, and modifications were made to the ground structure to reduce mutual coupling. The optimization method based on the trust-region algorithm is employed again to enhance the MIMO performance. The outcomes demonstrate outstanding performance metrics, including isolation levels over 32 dB and high gains exceeding 7 dBi at both frequency bands. Following the manufacturing and testing of the system, the simulation results were validated, affirming its exceptional performance. The designed MIMO system demonstrated exceptional isolation and gain, with a low-profile structure and simplified architecture, outperforming the recent MIMO devices reported in the literature. The contributions of this work are summarized as follows:

I. Design a dual-band antenna with a compact size and high gain, based on two interconnected patches that operate in the millimeter-wave spectrum.

II. Implementation of a four-port dual-band MIMO antenna, incorporating both a parasitic patch and ground modifications to achieve high isolation of more than 32 dB at both 28 GHz and 38 GHz.

III. Development and execution of a customized two-stage optimization approach to refine the individual antenna parameters, simultaneously ensuring a high reflection coefficient and high gain at both operating frequencies, and to enhance the MIMO isolation. The TR gradient-based search algorithm is employed to optimize the geometrical dimensional of the antenna and MIMO while maintaining a low profile and simplicity. For that purpose, a regularization-based objective function is defined, enabling simultaneous control over the single antenna gain and its reflection response, as well as the MIMO isolation and the reflection response.

The proposed MIMO system, offering dual-band functionality, omnidirectional coverage, and high gain, provides an effective solution to signal losses, multipath fading, and interference in 5G millimeter-wave indoor cellular communications. The subsequent sections of this work are organized as follows: Section "2- Dual band antenna design" introduces the dual-band antenna, followed by Section "3- Antenna Response Optimization", which elaborates on antenna performance optimization. In Section "4- MIMO antenna", the MIMO antenna configuration is presented, while Section "5- MIMO Response Optimization" discusses MIMO response optimization. The experimental validation of the system is detailed in Section "6- Experimental Validation", while its performance is discussed in Section "7- MIMO Performance". Section "8- Conclusions" concludes the paper.

Dual band antenna design

The dual band antenna configuration is shown in (Fig. 1). The fundamental structure of the antenna comprises a circular patch with a radius R_m, which can be calculated using the following expressions[31]:

$$R_m = \frac{K}{\sqrt{1 + \frac{2hs}{\pi \epsilon K}\left[ln\left(\frac{\pi K}{2hs}\right) + 1.7726\right]}} \tag{1}$$

$$K = \frac{8.791 \times 10^9}{f_r \sqrt{\epsilon}} \tag{2}$$

Here, ϵ and h_s represent the relative permittivity and thickness of the substrate, respectively. f_r is the circular patch resonant frequency. Two rings, with inner radius R_{m1} and outer radius R_{m2}, have been added to the sides along the x-axis to introduce inductive loading to the main patch. These extensions consist of two symmetric circular cuts. Furthermore, a slotted ellipse with major and minor radii of U_r and V_r, respectively, is incorporated

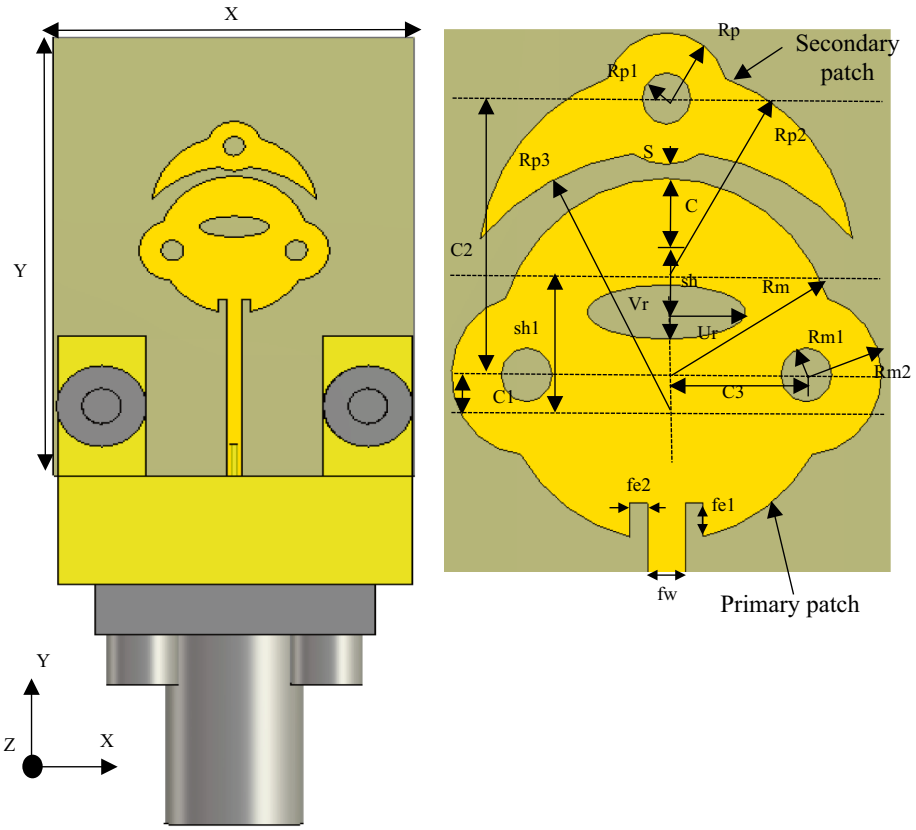

Fig. 1. The structure of the dual-band antenna; dimensions in mm, $X = 13$, $Y = 15$, $R_m = 2.728$, $R_{m1} = 0.406$, $U_r = 1.257$, $V_r = 0.410$, $S_h = 0.890$, $R_p = 0.990$, $R_{p1} = 0.387$, $R_{m2} = 1.198$, $S_{h1} = 2.243$, $f_{e2} = 0.284$, $f_{e1} = 0.466$, $C_1 = 0.65$, $C_2 = 4.15$, $C_1 = 2.24$, $S = 0.20$, $f_w = 0.60$.

on the upper side of the primary patch. The inclusion of this slot primarily aims to regulate impedance matching at 38 GHz, where the main patch is responsible for exciting this frequency. In other words, it is utilized to regulate the reflection coefficient magnitude and align the resonance at 38 GHz. The inset feeding technique is employed to excite the main circular structure. A secondary arc-shaped patch, serving as a capacitive load through the gap of width S, has been added over the main patch, positioned opposite to the feed. Before employing the optimization method, many simulations were conducted to optimize the gap S, which is a crucial factor in obtaining optimal results. The secondary patch consists of a circular ring with a radius R_p and is fed through coupling gap with the primary patch. The Rogers RT5880 substrate, characterized by a dielectric constant of 2.2, a tangent loss of 0.0009, and a thickness of 0.508 mm, was chosen for the antenna design. Figure 2(a) illustrates reflection coefficient. The dual-band property was accomplished by integrating two patches, as indicated by the reflection coefficient prior to optimization. Despite enabling dual-band capability, the two patches do not resonate at the desired bands of 28 and 38 GHz, as illustrated in Fig. 2(a). Further the bandwidth and gain need to be enhanced. Optimization holds promise for improving the antenna's performance. However, this entails conducting numerous electromagnetic simulations, which can take up considerable time and necessitate human involvement after every simulation. Employing numerical optimization can streamline the process of adjusting the dimensions of the antenna, thereby reducing time requirements. Given that the antenna's response typically hinges upon the accurate adjustment of its dimensions and accurate formulas are unavailable for the creation of all antenna configurations, the implementation of optimization techniques emerges as the optimal strategy to attain the desired outcome with minimal time and exertion. The trust-region optimization approach was utilized in this study to determine the ideal dimensions of the antenna and achieve the desired results. Section "3- Antenna Response Optimization" outlines the specifics of the optimization procedure. The design procedure for the proposed antenna, considering the described explanation and operating mechanism, is outlined as follows:

1 Design the main circular patch with an inset feed using the formula provided in (1).

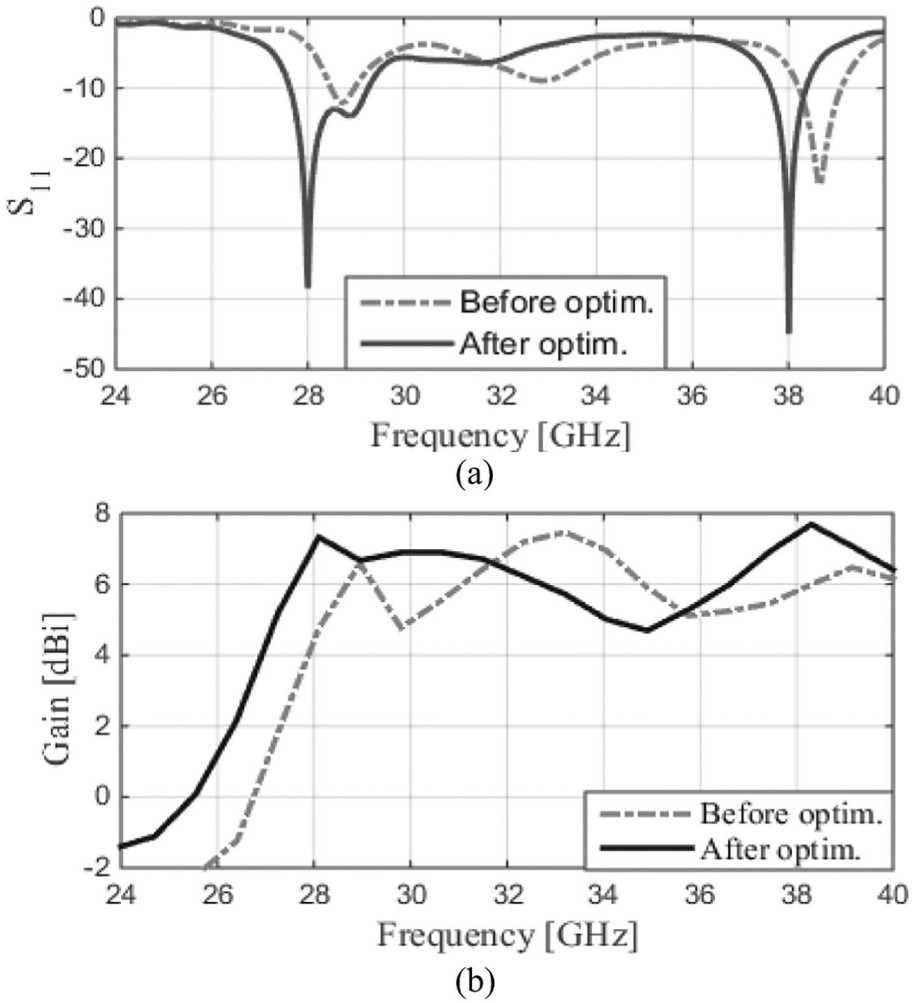

Fig. 2. Antenna performance pre and post optimization, (**a**) the reflection coefficient and (**b**) the gain.

2 Introduce a pair of symmetrical rings within the main patch, aligned along the x-axis, to induce inductive loading. Additionally, a slotted ellipse is implemented on the upper side of the primary patch to fine-tune impedance matching at 38 GHz, the excitation frequency of the main patch.
3 Introduce a secondary arc-shaped patch on top of the main patch, accompanied by a circular ring, to serve as a capacitive load through a gap with width S. The gap, S, is a crucial factor in achieving the dual-band result.
4 Employ the expedited trust-region (TR) algorithm to optimize the dimensions of the antenna components, ensuring that the antenna operates efficiently with high reflection and gain at both bands.

Antenna response optimization

The dual-band antenna is initially optimized as a standalone structure, focusing on enhancing the reflection coefficient performance (i.e., improving the impedance bandwidth). The optimization process employs the adjustable parameters $\boldsymbol{x} = [R_m\ R_{m1}\ U_r\ V_r\ S_h\ R_p\ R_{p1}\ R_{m2}\ S_{h1}\ f_{e2}\ f_{e1}]^T$, all elucidated in Fig. 1. The ranges defining the parameter space X are as follows: $2.5 \le R_m \le 2.8$ mm, $2.5 \le R_m \le 2.8$ mm, $0.3 \le R_{m1} \le 0.7$ mm, $0.7 \le U_r \le 1.4$ mm, $0.2 \le V_r \le 0.9$ mm, $0.7 \le S_h \le 1$ mm, $0.7 \le R_p \le 1$ mm, $0.3 \le R_{p1} \le 0.6$ mm, $1 \le R_{m2} \le 1.4$ mm, $1 \le S_{h1} \le 2.25$ mm, $0.2 \le f_{e2} \le 0.4$ mm, $0.2 \le f_{e2} \le 1$ mm. Additionally, the following geometry constraints were imposed upon the parameter vector $\boldsymbol{x}$: $R_p - R_{p1} \ge 0.2$ mm, and $U_r > V_r$. The primary objective is to enhance the reflection coefficient performance $|S_{11}(\boldsymbol{x},\boldsymbol{f})|$ at $f_1 = 28$ GHz and $f_2 = 38$ GHz. The secondary goal is to guarantee that $G(\boldsymbol{x},\boldsymbol{f}) \ge 7$ dBi at both f_1 and f_2. Considering the primary aim and the constraints, the cost function to be minimized is formally defined as follows.

$$U(x) = \max_{f \in \{f_1, f_2\}} \left\{ |S_{11}(x,f)| \right\} + \beta \left[\frac{\max\{7 - G_{\min}(x), 0\}}{7} \right]^2 \tag{3}$$

where

$$G_{\min}(x) = \min_{f \in \{f_1, f_2\}} \left\{ |G(x,f_1)|, |G(x,f_2)| \right\} \tag{4}$$

is the minimum of the in-band gain. The objective function U of (3) consists of two component, the first being the primary objective (impedance matching improvement), and second being a penalty term, which enforces the gain not to fall below 7 dB. The optimal design $\boldsymbol{x}^*$ is determined by solving a nonlinear minimization task

$$x^* = \arg\min_{x \in X} U(x) \tag{5}$$

The decrease in $U(\boldsymbol{x})$ corresponds to an improvement in impedance matching and the enforcement of the antenna gain condition. The second term in (3) is scaled according to the degree of violation of the condition $G(\boldsymbol{x},f) \ge 7$ dB, with the coefficient β[32] fixed at 100. This value ensures that violations exceeding a fraction of a dB will significantly contribute to the penalty term in U, promoting design adjustments towards compliance with the condition. At this juncture, it is crucial to highlight that implicitly addressing the gain-related constraint[33] is advisable due to its expensive computational nature, necessitating evaluation through EM simulation. The optimization process is based on the trust-region (TR) gradient-based algorithm[34], while the antenna response Jacobian matrix is estimated using finite differentiation[35]. The TR algorithm generates a sequence $x^{(i)}$, $i = 0, 1, \ldots$, of approximations to x^* as

$$x^{(i+1)} = \max_{\substack{x \in X \\ ||x - x^{(i)}|| \le d^{(i)}}} U_L^{(i)}(x) \tag{6}$$

The objective function $U_L^{(i)}$ in (6) is defined as in (3), albeit derived from the first-order linear approximation model of antenna characteristics. The sub-problem (6) aims at local optimization of the linear model, which represents antenna response in the vicinity of the current design $\boldsymbol{x}^{(i)}$. For illustration, concerning the reflection response:

$$L_{S_{11}}^{(i)}(x) = S_{11}(x,f) + \nabla S_{11}(x^{(i)},f) \cdot (x - x^{(i)}) \tag{7}$$

Here, $\nabla S_{11}(\boldsymbol{x}^{(i)},f)$ represents the gradient of the reflection response at design $\boldsymbol{x}^{(i)}$ and frequency f. In a comparable fashion, the linear model for the gain response is established. Note that the linear model is first-order consistent with the EM-simulated antenna responses, i.e., it agrees in terms of the EM-analysis outputs and its sensitivities at the current design. At the onset of each iteration, the size $d^{(i)}$ of the search region is modified according to standard TR procedures[32]. Termination of the algorithm occurs when convergence in argument is achieved, defined by the condition $||\boldsymbol{x}^{(i+1)} - \boldsymbol{x}^{(i)}|| < \varepsilon$; where $\varepsilon = 10^{-3}$. The initial design $\boldsymbol{x}^{(0)} = [2.7\ 0.35\ 1.15\ 0.3\ 0.75\ 0.35\ 0.9\ 0.35\ 1\ 2.1\ 0.2\ 0.35]^T$ mm was determined through parametric studies. Through optimization, the final design is established as $\boldsymbol{x}^* = [2.728\ 0.406\ 1.257\ 0.410\ 0.890\ 0.200\ 0.990\ 0.387\ 1.198\ 2.243\ 0.284\ 0.466]^T$ mm. The antenna reflection and gain responses for both the initial and optimized designs are shown in Fig. 2a,b. The reflection response at the lower band, 28 GHz, sees improvement after optimization in both magnitude (enhanced to −38 dB) and bandwidth, expanding to 2.7 GHz (26.6–29.3 GHz), cf. Figure 2a. At the same time, at 38 GHz, the reflection magnitude is further enhanced to −45 dB with a bandwidth of 0.75 GHz (37.6–38.35 GHz). In terms of the gain response, it increases from 4.4 dBi before optimization to 7.2 dBi after optimization at 28 GHz, and from 5.8 dBi to 7.4 dBi at 38 GHz. The effect of varying the coupling between the two patches, represented by S, on the antenna's reflection coefficient response is presented in Fig. 3. Numerical simulations were performed

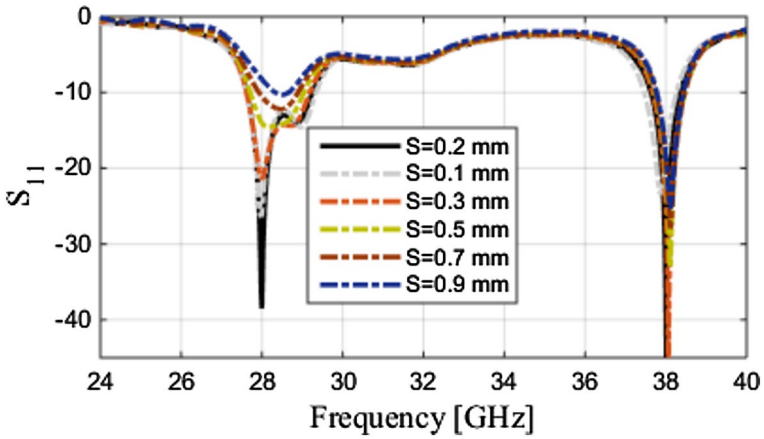

Fig. 3. Effect of changing the coupling between two patches, *S*, on the antenna reflection coefficient response.

with *S* values ranging from 0.1 to 0.9 mm, while other parameters were held constant as depicted in Fig. 1. Good impedance matching at 28 GHz is observed with lower *S* values, but values greater than 0.7 mm result in poor matching. Exceeding 0.7 mm causes the antenna to lose its dual-band capability, which is the main purpose of the secondary patch. Figure 3 clearly demonstrates that with *S* set to 0.2 mm, the resonance frequencies coincide with the desired frequencies of 28 and 38 GHz, and this value also adheres to fabrication constraints. Analyzing the surface current distribution on both the primary and secondary patches is essential for comprehending the radiation mechanism of the dual-band antenna at both bands. Figures 4a,b illustrate the current distributions at both 28 and 38 GHz, respectively. In Fig. 4a, the surface current predominantly resides on the primary patch, with an extension through the coupling slot to the secondary patch. This arrangement allows both patches to work together to attain the lower band frequency of 28 GHz. Conversely, at 38 GHz, only the primary patch exhibits surface current, particularly concentrated around the slot ellipse and slot circles, as presented in Fig. 4b. Dual-band operation is enabled by the composite structure of the antenna. The primary patch, in conjunction with the parasitic arc-shaped patch, handles radiation at the first band of 28 GHz. On the contrary, radiation at 38 GHz is solely facilitated by the primary patch.

MIMO antenna

As previously mentioned, MIMO technology holds promise in augmenting communication systems by refining link quality and counteracting multipath fading effects. The inclusion of the dual-band property can extend these improvements. This section introduces a MIMO antenna featuring four dual-band elements organized in an orthogonal layout. In this setup, the mutual coupling is low across both frequency bands, coupled with outstanding diversity performance compared to series and opposite orientations. It adeptly mitigates the drawbacks of series and opposite arrangements by ensuring radiating elements are suitably spaced to bolster the overall system isolation. Figure 5a presents the developed MIMO system, built on a Rogers substrate, compactly

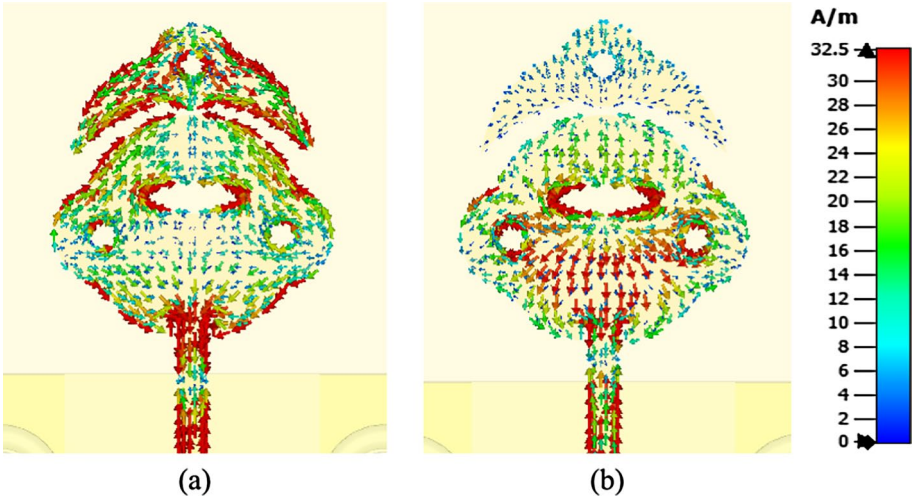

Fig. 4. Current distributions at (**a**) 28 GHz and (**b**) 38 GHz.

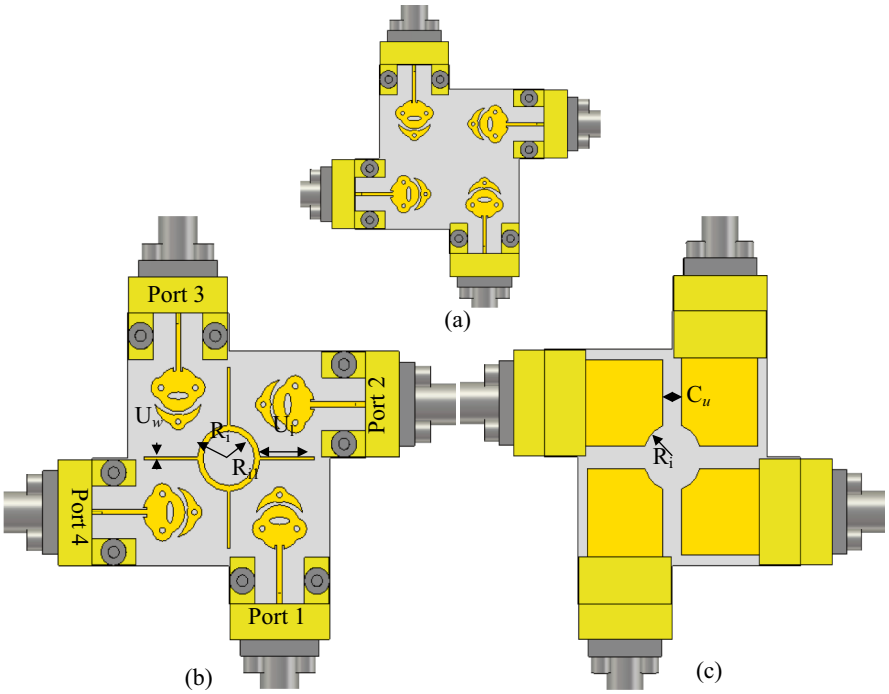

Fig. 5. The developed MIMO system (**a**) without isolation enhancement technique, (**b**) with parasitic patch in front view, and (**c**) modified ground in back view; dimensions in mm, $R_i = 3.789$, $R_{i1} = 3.208$, $U_w = 0.527$, $U_l = 3.208$, $C_u = 2.987$, $R_m = 2.662$, $R_{m2} = 1.278$, $S_h = 0.7005$, $U_r = 1.399$, $V_r = 0.625$.

sized at $28 \times 28 \times 0.508$ mm^3. The simulated reflection and transmission coefficients are depicted in Fig. 6. The reflection coefficient closely mirrors that of a single antenna. As for the transmission coefficients, the proposed system provides good isolation at both bands, surpassing 19 dB, whereas the series arrangement demonstrates only 16 dB. Constructing a reliable MIMO system capable of operating at millimeter-wave frequencies necessitates minimizing mutual coupling. Consequently, this study employs a parasitic patch on the front side and modifies the ground on the back view to achieve this objective. Figures 5b,c illustrate the fore and rear views of the MIMO system with the coupling reduction technique applied. As part of the isolation enhancement, a ring with four copper strips has been introduced as a parasitic element, positioned in the middle between the four elements. Additionally, modifications have been made to the ground by reducing its dimensions as well as incorporating a circular cut in the center of the ground. These adjustments ensure that the ground is appropriately modified, maintaining sufficient spacing between the grounds to mitigate high mutual coupling. The reflection and transmission coefficients of the MIMO system, after incorporating the isolation enhancement technique, are illustrated in Fig. 7. It is evident that the isolation has been enhanced in comparison to the bare MIMO system, cf. Figure 6. This suggests that further enhancement in isolation can be achieved by optimizing the parameters of the parasitic patch and ground dimensions. However, this process typically involves manual adjustments by human operators after each simulation, which can be time-consuming due to the large size of the model and the time required to complete each simulation, rendering traditional optimization procedures impractical. Numerical

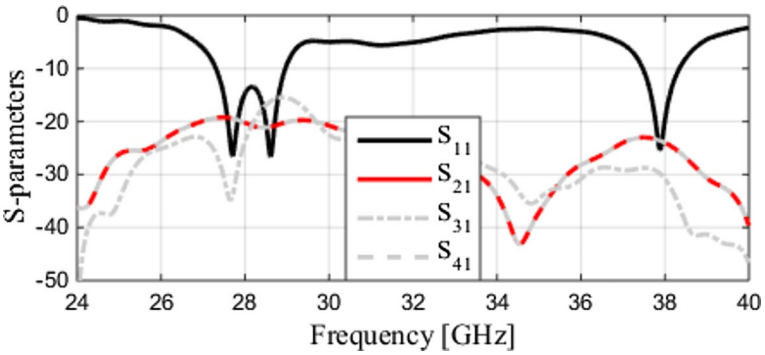

Fig. 6. The S-parameters of the MIMO without coupling reduction technique.

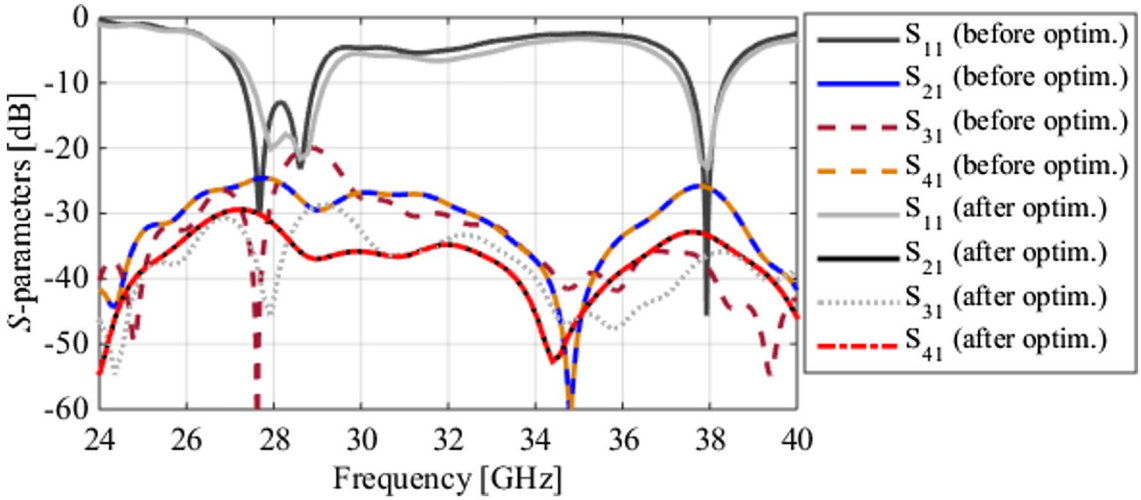

Fig. 7. *S*-parameters of the dual-band MIMO system with parasitic patch and modified ground before and after optimization.

optimization emerges as the preferred method for controlling parameters and achieving the desired isolation results efficiently. In this study, the trust-region optimization approach was employed once again to optimize the dimensions of the parasitic patch and ground and attain the desired isolation. Section "5- MIMO Response Optimization" outlines the specifics of this optimization process. According to the described explanation, the design methodology for the proposed high-isolation MIMO system is as follows:

(1) Implement four dual-band elements in an orthogonal layout. Various MIMO arrangements were studied, and the orthogonal orientation was selected for its lower mutual coupling compared to other configurations.
(2) Introduce a ring with four copper strips as a parasitic element, placed centrally between the four elements to reduce mutual coupling.
(3) Modify the ground by reducing its dimensions and incorporating a circular cut at its center. These changes ensure that the ground maintains adequate spacing between the elements to mitigate high mutual coupling.
(4) Apply the trust-region optimization approach again to fine-tune the dimensions of the parasitic patch and ground, ensuring that the target isolation is realized

MIMO response optimization

Optimization of the MIMO version of the proposed dual-band antenna aims to enhance antenna isolation $|S_{ij}|$ at frequencies $f_1 = 28$ GHz and $f_2 = 38$ GHz. Further stipulations necessitate maintaining sufficient reflection with $|S_{11}(x,f)| \leq -20$ dB and ensuring a gain of $G(x,f) \geq 7$ dB at both frequencies. For optimization, the design variables selected are $\boldsymbol{x} = [R_i\ R_{i1}\ U_w\ U_l\ C_u\ R_m\ R_{m2}\ S_h\ U_r\ V_r]^T$. The initial five parameters are derived from the isolation reduction technique (circular path and modified ground), as illustrated in Fig. 5b,c. The remaining parameters pertain to the fundamental dual-band antenna and are recycled in the second stage of optimization to provide additional degrees of freedom for controlling the reflection and gain. The following ranges determine the parameter (search) space X: $3.5 \leq R_i \leq 5$ mm, $2 \leq R_{i1} \leq 3.8$ mm, $5 \leq U_l \leq 7.2$ mm, $0.4 \leq U_w \leq 1.7$ mm, $0.2 \leq C_u \leq 3$ mm, $2.5 \leq R_m \leq 2.8$ mm, $1 \leq R_{m2} \leq 1.4$ mm, $0.6 \leq S_h \leq 1.1$ mm, $0.7 \leq U_r \leq 1.4$ mm, $0.2 \leq V_r \leq 0.9$ mm. Furthermore, two geometry constraints are considered: $R_i - R_{i1} > 0.2$ and $R_i + U_l < 11.4$ mm (to avoid the parasitic patch strips from touching the end-launch connector). The lower boundaries of both parameters indicate that values below these thresholds have minimal impact on isolation performance. This was determined through parametric studies conducted before optimization. The principal aim is to increase the antenna's mutual coupling, represented by $M(\boldsymbol{x}) = max\{f \in \{f_1, f_2\}, j = 1, i \in \{2,3,4\} : |S_{ij}(\boldsymbol{x}, f)|$. Considering the remaining conditions as constraints, the resulting objective function to minimize is thus defined as

$$U_1(\boldsymbol{x}) = M(\boldsymbol{x}) + \beta_1 \left[\frac{\max\{S_{max}(\boldsymbol{x}) + 20,0\}}{20}\right]^2 + \beta_2 \left[\frac{\max\{G_{min}(\boldsymbol{x}) - 7,0\}}{7}\right]^2 \quad (8)$$

where $S_{\max}(\boldsymbol{x}) = \max\{f \in \{f_1 f_2\} : |S(\boldsymbol{x},f)|\}$, whereas $G_{min}(\boldsymbol{x})$ has been defined in (4). Both constraints are of the the inequality type, with their violations quantified as relative values. The penalty coefficients are set to $\beta_1 = \beta_2 = 100$. Note that at this stage of the optimization process, the main objective is to reduce the mutual coupling $M(\boldsymbol{x})$, while fulfilling the conditions concerning impedance matching (to be better than -20 dB) and gain (not to fall below 7 dB). Through parametric studies, the initial design is $\boldsymbol{x}^{(0)} = [4\ 3.3\ 0.4\ 6.9\ 2.6\ 2.728\ 1.198\ 0.890\ 0.406\ 1.257]^T$, with the exclusion of the last five variables, inherited from the initial optimization iteration. Through the use of the trust-region algorithm described earlier, the optimized design $\boldsymbol{x}^* = [3.789\ 3.208\ 0.527\ 3.208\ 2.987\ 2.662\ 1.278$

0.700 1.399 0.625]^T has been obtained by minimizing the objective function (7) similar to (6). Figure 7 displays the transmission coefficients and isolation of the dual-band MIMO system with parasitic patch and modified ground both before and after optimization. Notably, the isolation is observed to improve from over 25 dB before optimization to over 32 dB at 28 GHz and 33.5 dB at 38 GHz after optimization. The reflections are better than −20 dB owing to the constraint outlined in the optimization. To demonstrate the effect of the decoupling structure on mutual coupling reduction, the surface current is analyzed. Figure 8 illustrates the surface current distributions for the dual-band MIMO antenna, with and without decoupling structures, at both 28 and 38 GHz. During the analysis, Port 1 is excited and Ports 2 through 4 are terminated with a 50-Ω load. Without decoupling structures, there is considerable mutual coupling at Antennas 2 through 4 at both 28 and 38 GHz, as shown in Figs. 8a,c. However, incorporating a parasitic patch and ground modifications significantly reduces the coupling current at Antennas 2 through 4, as illustrated in Figs. 8b, d, thus enhancing isolation at both bands.

Experimental validation

The quad-port MIMO antenna was manufactured to validate the numerical simulation results and demonstrate its suitability for 5G systems. Figures 9a,b showcase the fore and rear views of the fabricated MIMO. Measurements of the reflection and transmission coefficients were conducted using the Anritsu vector network analyzer MS4644B. The radiation patterns were verified in the anechoic chamber, as displayed in Fig. 9c. The reflection coefficients of the quad-port system, considering the ground modifications and the addition of a parasitic patch, obtained from both simulation and measurement, are presented in Fig. 10. The outcomes are based on a single port, given that the antenna elements demonstrate identical and symmetrical characteristics. A satisfactory consistency between both datasets can be noted, especially in bandwidth. However, the reflection magnitude is lower in the measurement data, which can be attributed to fabrication tolerances, loss in the cable, and the use of bulky connectors. On the other hand, by introducing a parasitic patch and reducing the ground dimensions of the MIMO antenna, isolation has been enhanced, as depicted in Fig. 11. The measured mutual coupling between the four ports, $|S_{21}|$, $|S_{31}|$, and $|S_{41}|$, closely resembles the simulation, thereby confirming that the proposed MIMO provides isolation exceeding 30 dB at both 28 and 38 GHz bands. Nonetheless, minor variations in the resonant magnitudes exist between the measured results and the simulation. The gain plots are presented in Fig. 12. In the measurement, Port 1 is activated and other ports are connected to 50-Ω load. At the lower band, 28 GHz, the simulated realized gain is 7 dBi, while the measured gain is 6.8 dBi. Likewise, at the upper band of 38 GHz, the simulated realized gain is 7.9 dBi, and the measured gain is 7.4 dBi. These measured values closely match the numerical simulation results, particularly at the lower band, although there are slight deviations at

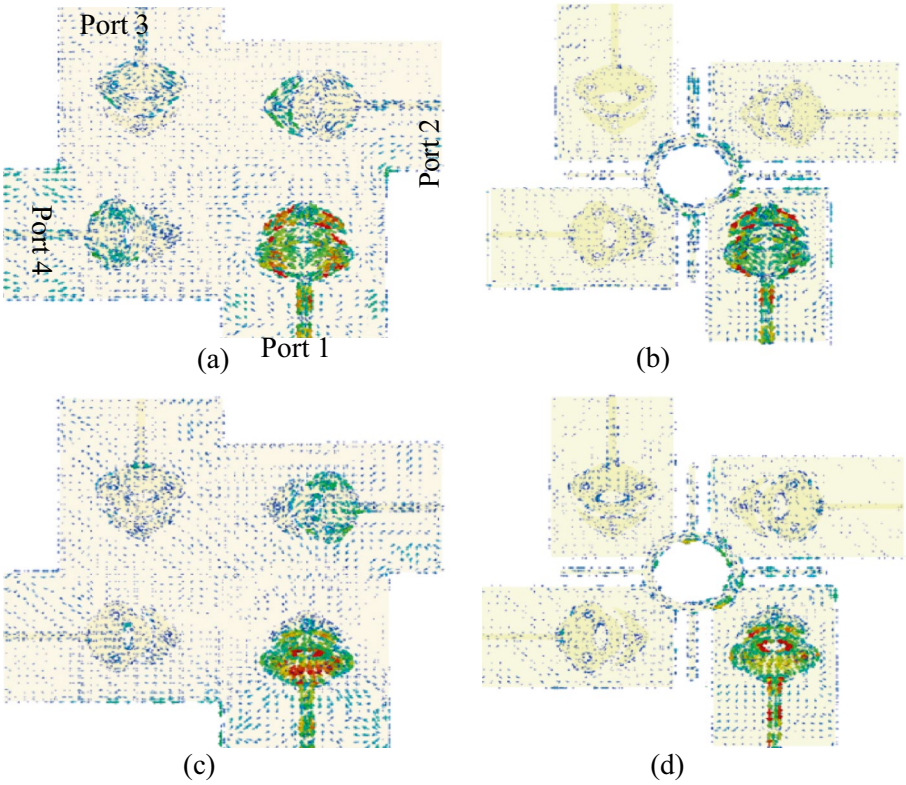

Fig. 8. The surface current distribution of the MIMO system at Port 1, (**a**) and (**b**) the currents with and without the decoupler structure at 28 GHz, and (**c**) and (**d**) show the currents with and without the decoupler structure at 38 GHz.

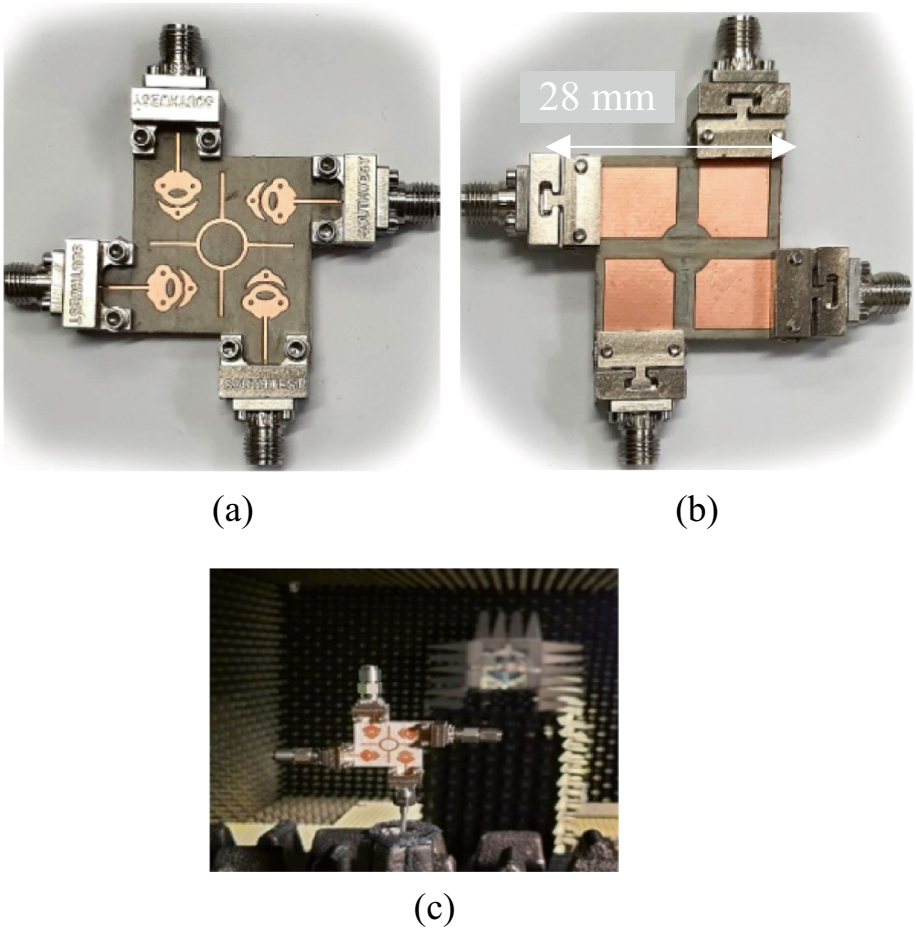

Fig. 9. Fabricated MIMO system, (**a**) front view and (**b**) back view, and (**c**) radiation pattern measurement setup.

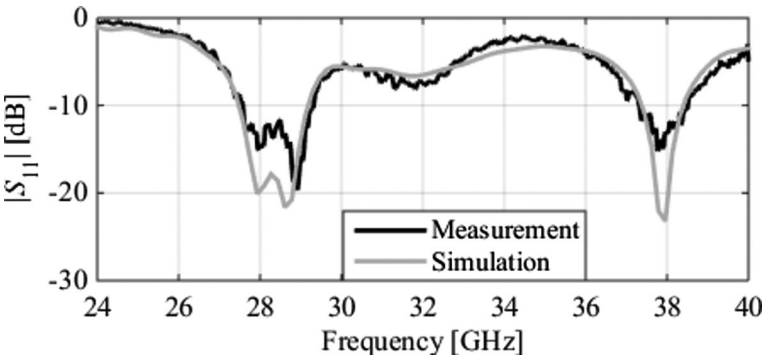

Fig. 10. Simulated and measured $|S_{11}|$ of the developed MIMO.

the upper band. Figures 13a,b display the E-plane and H-plane radiation patterns at 28 and 38 GHz, respectively. Throughout the measurement, the first antenna, Port 1, of the developed MIMO system is activated, while the other elements are terminated with a standard 50-Ω load. The E-plane and H-plane demonstrate non-uniform omnidirectional radiation patterns at both frequency bands. Additionally, the MIMO system exhibits low cross-polarization levels, particularly in the E-plane at both frequency bands.

MIMO performance

Evaluating a MIMO system's effectiveness involves considering the correlation between MIMO ports. This study delves into the analysis of the developed quad-port MIMO, considering various parameters such as the envelope correlation coefficient (ECC), channel capacity loss (CCL), diversity gain (DG), and total active reflection

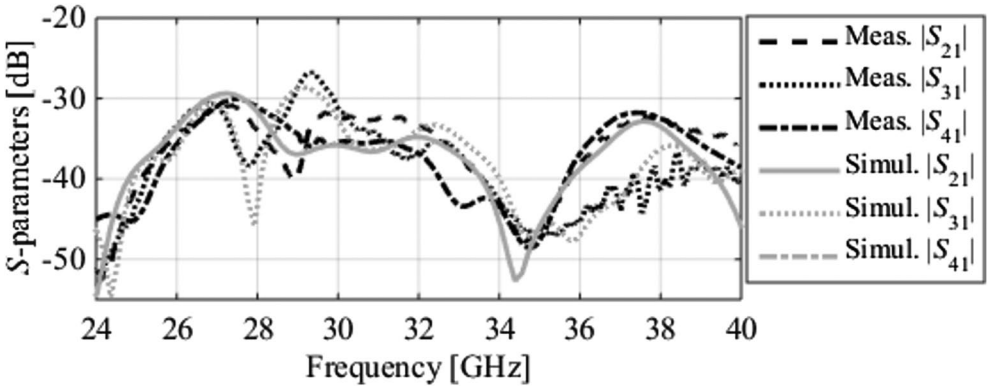

Fig. 11. Simulated and measured $|S_{21}|$, $|S_{31}|$, and $|S_{41}|$ of the developed MIMO.

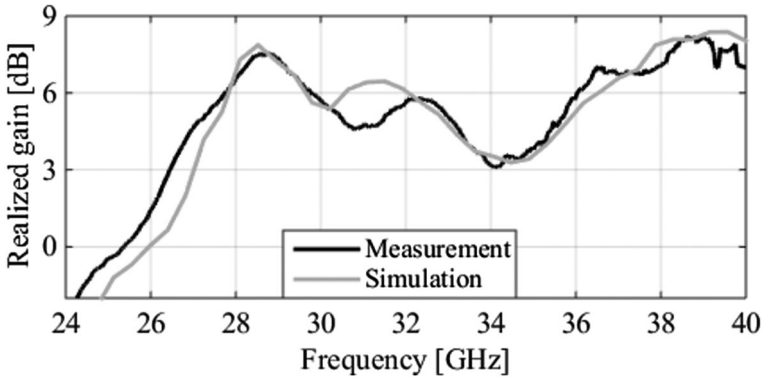

Fig. 12. Simulated and measured gain.

coefficient (TARC). The ECC quantifies the correlation among MIMO elements, ideally reaching zero, with a practical threshold typically below 0.5[36]. It is computed from S-parameters using the following expression[37].

$$ECC_{ij} = \frac{\left|S_{ii}^{*}S_{ij} + S_{ji}^{*}S_{jj}\right|^{2}}{(1-(|S_{ii}|^{2}+|S_{ji}|^{2}))(1-(|S_{jj}|^{2}+|S_{ij}|^{2}))} \tag{9}$$

ECC_{ij} denotes the correlation between the ith and jth MIMO elements. ECC is calculated from the farfield as follows[23]:

$$ECC_{ij} = \frac{\left|\iint_{4\pi}[E_i(\theta,\varphi) * E_j(\theta,\varphi)]d\Omega\right|^{2}}{\iint_{4\pi}|E_i(\theta,\varphi)|^{2}d\Omega \iint_{4\pi}|E_j(\theta,\varphi)|^{2}d\Omega} \tag{10}$$

$E_i(\theta,\varphi)$ characterizes the 3D radiation pattern when antenna i is activated and $E_j(\theta,\varphi)$ does the same for antenna j when it is activated. Figure 14a displays the ECC plots derived from S-parameters and far-field of the four-port MIMO system. The ECC values derived from both methods demonstrate close alignment within the desired bandwidth, showing ECC levels below 0.0005 at both bands. This comfortably meets the wireless network requirement of ECC < 0.5. Unlike a single antenna, the boost in signal-to-noise ratio (SNR) with multiple antennas is explained by diversity gain. This can be evaluated from ECC by[38]

$$DG = 10 \times \sqrt{1-\left|ECC_{ij}\right|^{2}} \tag{11}$$

Typically, higher DG values suggest enhanced MIMO performance. DG depicted in Fig. 14(b) shows elevated levels at 28 and 38 GHz, nearing the 10 dB standard. TARC, representing the ratio of the square root of the total reflected power to the square root of the total incident power, is a crucial consideration in MIMO performance evaluation. It helps identify MIMO operating bands and radiation performance adjustments when modifying input signal phases. The calculation of the TARC for the four elements can be carried out using the following expression[39]

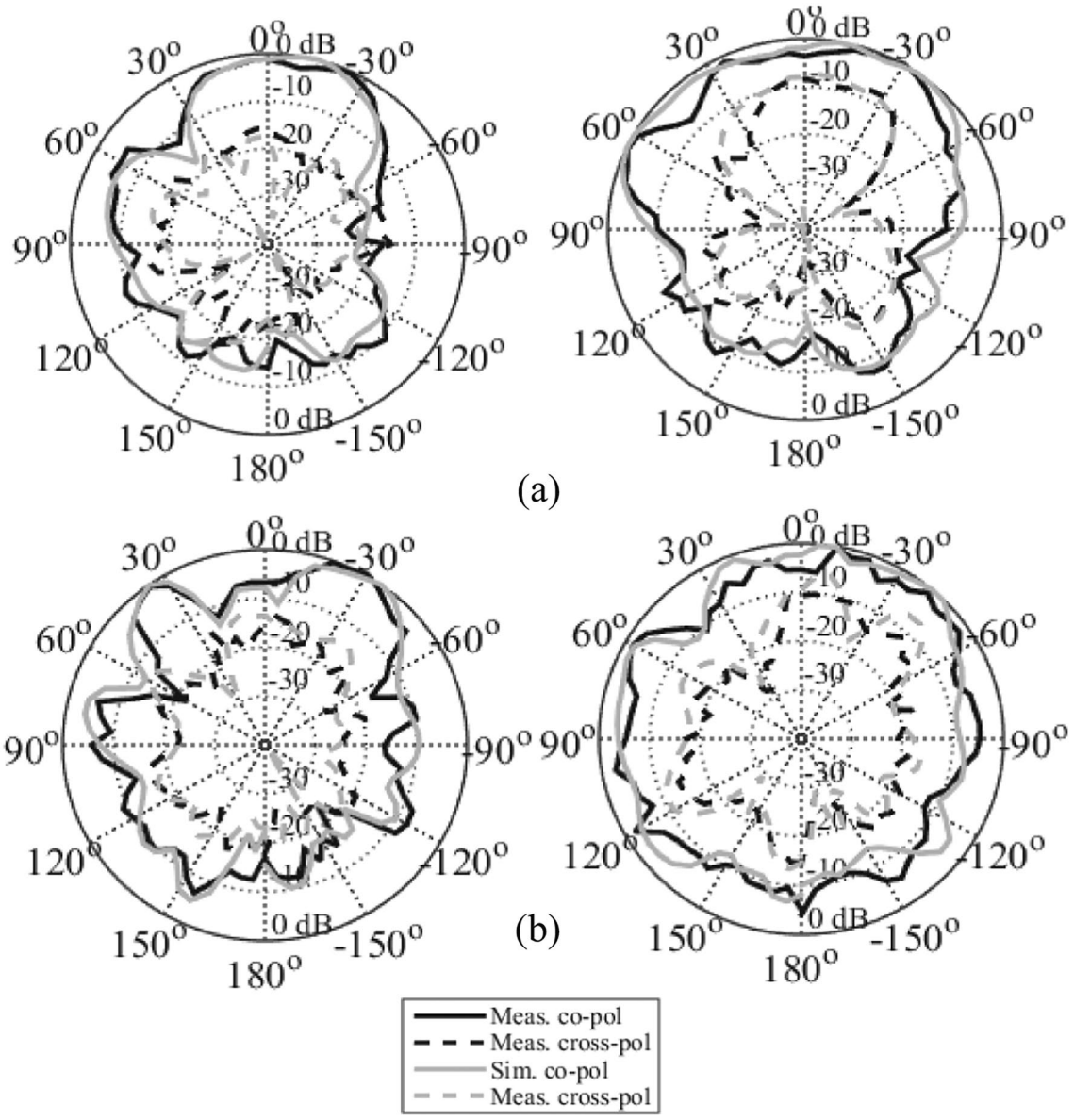

Fig. 13. Simulated and measured E- and H-plane radiation patterns at (**a**) 28 GHz and (**b**) 38 GHz.

$$TARC = \sqrt{\frac{\left|S_{11} + S_{12}e^{j\theta_1} + S_{13}e^{j\theta_2} + S_{14}e^{j\theta_3}\right|^2 + \left|S_{21} + S_{22}e^{j\theta_1} + S_{23}e^{j\theta_2} + S_{24}e^{j\theta_3}\right|^2 + \left|S_{31} + S_{32}e^{j\theta_1} + S_{33}e^{j\theta_2} + S_{34}e^{j\theta_3}\right|^2 + \left|S_{41} + S_{42}e^{j\theta_1} + S_{43}e^{j\theta_2} + S_{44}e^{j\theta_3}\right|^2}{4}} \quad (12)$$

The TARC is depicted in Fig. 15a, with a clear indication that it remains under −10 dB in both operating bands. The CCL is primarily concerned with identifying the optimal transmission capacity of a communication link while mitigating data loss. Ensuring the efficiency of a MIMO antenna system involves maintaining the CCL below 0.4 bit/s/Hz. The CCL is mathematically represented as[30]

$$CCL = -\log_2 \det(\gamma) \quad (13)$$

Where ɣ is the correlation matrix,

$$\gamma = \begin{bmatrix} \gamma_{11} & \gamma_{12} & \gamma_{113} & \gamma_{14} \\ \gamma_{21} & \gamma_{22} & \gamma_{23} & \gamma_{24} \\ \gamma_{31} & \gamma_{32} & \gamma_{33} & \gamma_{34} \\ \gamma_{41} & \gamma_{42} & \gamma_{43} & \lambda_{44} \end{bmatrix} \quad (14)$$

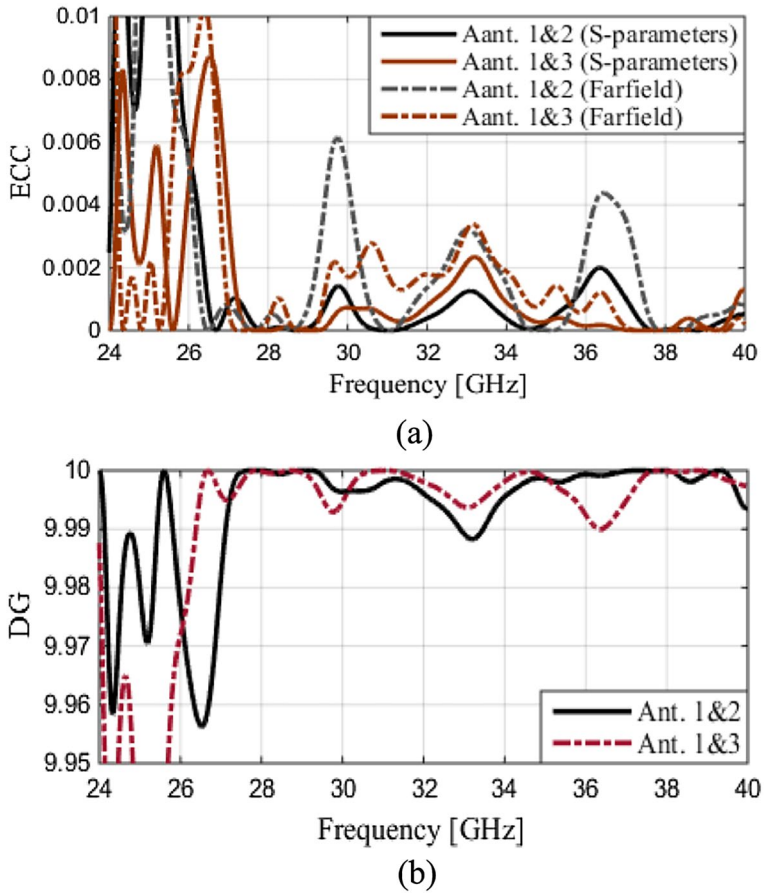

Fig. 14. MIMO performance of the proposed antenna, (**a**) ECC, (**b**) DG.

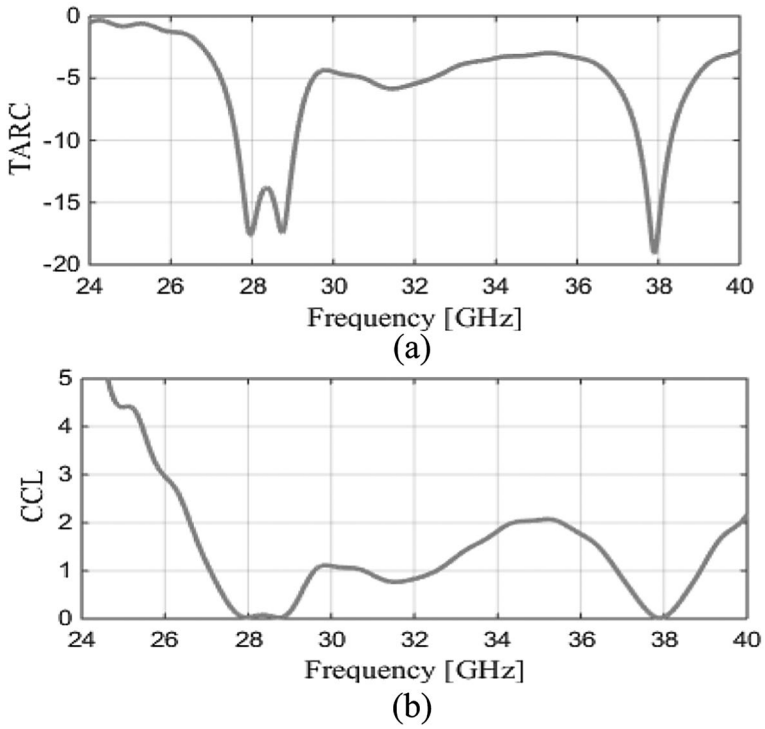

Fig. 15. The developed MIMO performance, (**a**) TARC, and (**b**) CCL.

Ref	Antenna structure (No. of ports)	Frequency (GHz)	Isolation (dB)	Gain (dBi)	ECC DG (dB)	CCL. (bits/s/H)	Decoupling structure
[13]	Monopole antenna (2)	27 and 39	> 25	(5) 28 GHz and (5.7) 38 GHz	−(10^{-4}) −(9.99)	–	–
[14]	Patch antenna (4)	27.1 and 48.7	> 27	(6) 27.1 GHz and 48.7 GHz	−(10^{-5}) −(9.99)	0.03	–
[15]	Monopole antenna (2)	28 and 38	> 20	(5.2) 28 GHz and (5.3) 38 GHz	−(10^{-5}) −(__)	–	–
[21]	Patch antenna (2)	28 and 38	> 28	(7) 28 GHz and (6) 38 GHz	−(< 0.001) −(9.99)	0.05	Metamaterials and ground modification
[26]	Patch antenna (2)	28	> 23	9	−(< 0.005) −(9.99)	0.3	Parasitic C patch
[27]	DRA (2)	28	> 24	8.1	−(< 0.148) −(9.89)	–	Parasitic metal strip patch
[28]	Circular patch antenna (2)	16	> 26	7.6	−(< 0.148) −(9.9)	–	Parasitic patch
[30]	Tilted spade-shaped antenna (4)	23.9–40.1	> 26	3–5	−(< 0.04) −(9.6–10)	< 0.25	Two cross lines
This work	Patch antenna (4)	28 and 38	> 32	(7) 28 GHz and (7.9) 38 GHz	−(< 0.0005) −(> 9.99)	0.03	Parasitic patch and ground modification

Table 1. Comparison between the proposed dual-band MIMO system and recent literature reports.

$$\gamma_{ii} = 1 - \sum_{j=1}^{2} |S_{ij}|^2 \tag{15}$$

As depicted in Fig. 15b, the MIMO system demonstrates CCL values that are below the standard of 0.4 bit/s/Hz. Table 1 presents a comprehensive comparison of the performance of the proposed quad-port MIMO antenna with that of cutting-edge structures delineated in recent literature. Unlike previous investigations, our newly devised MIMO antenna achieves the utmost isolation while sporting a compact, low-profile structure, superior gain, and remarkable diversity characteristics.

Conclusions

A dual-band MIMO antenna tailored for achieving high isolation and gain in 5G millimeter-wave indoor applications has been developed. The proposed antenna comprises two interconnected patches. The primary patch is circular, connecting to the inset feed, whereas the secondary patch is a parasitic arc placed over the upper main patch in the opposite direction of the feed. A gradient-based algorithm, incorporating numerical derivatives, was employed to refine antenna parameters, simultaneously ensuring a high reflection coefficient and high gain at both frequency bands. The antennas operate in dual bands at 28 and 38 GHz, exhibiting high gain exceeding 7 dBi at both frequencies. Subsequently, a MIMO system was set up with four radiators positioned orthogonally. This arrangement aids in reducing mutual coupling to below −19 dB at both bands. To further enhance isolation, both a parasitic patch and modifications to the ground were implemented. The trust-region method was once again employed to optimize the MIMO parameters, ensuring the best isolation results. The isolation was heightened to more than 32 dB at 28 GHz and 33.5 dB at 38 GHz. The developed MIMO exhibits outstanding diversity performance, as evidenced by the low ECC, TARC, and CCL metrics, coupled with high DG values. Experimental validation of the MIMO demonstrated consistency between simulated and measured data.

Data availability

All data has been included in study.

Received: 26 March 2024; Accepted: 26 August 2024
Published online: 03 September 2024

References

1. Ancans, G., Bobrovs, V., Ancans, A. & Kalibatiene, D. Spectrum considerations for 5G mobile communication systems. *Proc. Comput. Sci.* **104**, 509–5169 (2017).
2. Li, J., Matos, C. & Ghalichechian, N. A low-cost vertically integrated antenna array at 60 GHz with 85% efficiency. *IEEE Antennas Wirel. Propag. Lett.* **20**, 513–517 (2021).
3. Esmail, B. A. F., Koziel, S., Pietrenko-Dabrowska, A. & Isleifson, D. wideband high-gain low-profile series-fed antenna integrated with optimized metamaterials for 5G millimeter wave applications. *Sci. Rep.* **14**, 185 (2024).
4. Elsharkawy, R. R., Hussein, K. F. & Farahat, A. E. Dual-band (28/38 GHz) compact MIMO antenna system for millimeter-wave applications. *J. Infrared, Milli. Terahz. Waves* **44**, 1016–1037 (2023).
5. Hussain, M. *et al.* Isolation improvement of parasitic element-loaded dual-band MIMO antenna for Mm-wave applications. *Micromachines* **13**, 1918 (2022).
6. Cuneray, K., Akcam, N., Okan, T. & Arican, G. O. 28/38 GHz dual-band MIMO antenna with wideband and high gain properties for 5G applications. *AEU - Int. J. Electron. Commun.* **162**, 154553 (2023).

7. Ali, S. A., Wajid, M., Kumar, A. & Alam, M. S. Design challenges and possible solutions for 5G SIW MIMO and phased array antennas: A review. *IEEE Access* **10**, 88567–88594 (2022).
8. Chaturvedi, D., Kumar, A. & Raghavan, S. A nested SIW cavity-backing antenna for Wi-Fi/ISM band applications. *IEEE Trans. Antennas Propag.* **67**, 2775–2780 (2019).
9. Kumar, A. Substrate integrated waveguide cavity-backed slot antenna with low cross-polarization over the full bandwidth. *Microw. Opt. Technol. Lett* **66**, e34019 (2024).
10. Chaturvedi, D., Kumar, A. & Althuwayb, A. A. A dual-band dual-polarized SIW cavity-backed antenna-duplexer for off-body communication. *Alex. Eng. J.* **64**, 419–426 (2023).
11. Dicandia, F. A., Genovesi, S. & Monorchio, A. Analysis of the performance enhancement of MIMO systems employing circular polarization. *IEEE Trans. Antennas Propag.* **65**, 4824–4835 (2017).
12. He, M. *et al.* Is multipath channel beneficial for wideband massive MIMO with low-resolution ADCs?. *IEEE Trans. Commun.* **69**, 4083–4097 (2021).
13. Ali, W. *et al.* Planar dual-band 27/39 GHz millimeter-wave MIMO antenna for 5G applications. *Microsyst. Technol.* **27**, 283–292 (2021).
14. Jetti, C. R. *et al.* Design and analysis of modified U-shaped four element MIMO antenna for dual-band 5G millimeter wave applications. *Micromachines* **14**, 1545 (2023).
15. Sabek, A. R., Ali, W. A. & Ibrahim, A. A. Minimally coupled two-element MIMO antenna with dual band (28/38 GHz) for 5G wireless communications. *J. Infrared, Milli., and Terahz. Waves* **43**, 335–348 (2022).
16. Hasan, M. N., Bashir, S. & Chu, S. Dual band omnidirectional millimeter wave antenna for 5G communications. *J. Electromagn. Waves Appl.* **33**, 1581–1590 (2019).
17. Farahat, A. E. & Hussein, K. F. Dual-band (28/38 GHz) wideband MIMO antenna for 5G mobile applications. *IEEE Access* **10**, 32213–32223 (2022).
18. Elfergani, I., Rodriguez, J., Iqbal, A., Sajedin, M., Zebiri, C. and AbdAlhameed, R.A. Compact millimeter-wave MIMO antenna for 5G applications. *European Conference on Antennas and Propagation (EuCAP)*, Copenhagen, Denmark, 2020, March 15–20.
19. Kamal, M. M. *et al.* Infinity shell shaped MIMO antenna array for mm-wave 5G applications. *Electronics* **10**, 165 (2021).
20. Esmail, B. A. & Koziel, S. High isolation metamaterial-based dual-band MIMO antenna for 5G millimeter-wave applications. *AEU - Int. J. Electron. Commun.* **158**, 154470 (2023).
21. Khan, D., Ahmad, A. & Choi, D. Y. Dual-band 5G MIMO antenna with enhanced coupling reduction using metamaterials. *Sci. Rep.* **14**, 96 (2024).
22. Kumar, N., Kommuri, U. K. & Usha, P. Mutual coupling reduction in multiband MIMO antenna using cross-slot fractal multiband EBG in the E-plane. *Progress Electromagn. Res. C* **132**, 1–10 (2023).
23. Iqbal, A. *et al.* Electromagnetic bandgap backed millimeter-wave MIMO antenna for wearable applications. *IEEE Access* **7**, 111135–111144 (2019).
24. Sehrai, D. A. *et al.* Metasurface-based wideband MIMO antenna for 5G millimeter-wave systems. *IEEE Access* **9**, 125348–125357 (2021).
25. Esmail, B. A. & Koziel, S. Design and optimization of metamaterial-based dual-band 28/38 GHz 5G MIMO antenna with modified ground for isolation and bandwidth improvement. *IEEE Antennas Wirel. Propag. Lett.* **22**, 1069–1073 (2022).
26. Awan, W. A. *et al.* Enhancing isolation performance of tilted beam MIMO antenna for short-range millimeter wave applications. *Heliyon* https://doi.org/10.1016/j.heliyon.2023.e19985 (2023).
27. Zhang, Y., Deng, J. Y., Li, M. J., Sun, D. & Guo, L. X. A MIMO dielectric resonator antenna with improved isolation for 5G mm-wave applications. *IEEE Antennas Wirel. Propag. Lett.* **18**(4), 747–751 (2019).
28. Yon, H. *et al.* Development of C-shaped parasitic MIMO antennas for mutual coupling reduction. *Electronics* **10**, 2431 (2021).
29. Islam, T., Alsaleem, F., Alsunaydih, F. N. & Alhassoon, K. Mutual coupling reduction in compact MIMO antenna operating on 28 GHz by using novel decoupling structure. *Micromachines* **14**, 2065 (2023).
30. Rosaline, I., Kumar, A., Upadhyay, P. & Murshed, A. H. Four element MIMO antenna systems with decoupling lines for high-speed 5G wireless data communication. *Int. J. Antennas Propag.* **2022**, 9078929 (2022).
31. Balanis, C. A. *Antenna Theory: Analysis and Design* (John Wiley&sons, 2016).
32. Koziel, S., Pietrenko-Dabrowska, A. & Mahrokh, M. On decision-making strategies for improved-reliability size reduction of microwave passives: Intermittent correction of equality constraints and adaptive handling of inequality constraints. *Knowl Based Syst.* **255**, 1–16 (2022).
33. Koziel, S. & Pietrenko-Dabrowska, A. Reliable EM-driven size reduction of antenna structures by means of adaptive penalty factors. *IEEE Trans. Ant. Propag.* **70**, 1389–1401 (2021).
34. Conn, A. R., Gould, N. I. & Toint, P. L. *Trust region methods MPS-SIAM Series on Optimization* (Society for Industrial and Applied Mathematics, 2000).
35. Levy, H. & Lessman, F. *Finite difference equations* (Dover Publications Inc., 1992).
36. Esmail, B. A., Koziel, S. & Pietrenko-Dabrowska, A. Design and optimization of a compact super-wideband MIMO antenna with high isolation and gain for 5G applications. *Electronics* **12**, 4710 (2023).
37. Wang, H. & Wu, P. Wideband MIMO antennas for 5G mobile terminals. *IEEE Open J. Antennas Propag.* **4**, 74–80 (2023).
38. Khan, A., He, Y., He, Z. & Chen, Z. N. A compact quadruple-band circular polarized MIMO antenna with low mutual coupling. *IEEE Trans Circuits Syst. II: Express Br.* **70**, 501–505 (2022).
39. Musaed, A. A. *et al.* High isolation 16-port massive MIMO antenna based negative index metamaterial for 5G mm-wave applications. *Sci Rep.* **14**, 290 (2024).

Acknowledgements

This work was partially supported by the Icelandic Centre for Research (RANNIS) Grant 217771 and by National Science Centre of Poland Grant 2020/37/B/ST7/01448.

Author contributions

Conceptualization, B.A.F.E (Bashar A.F. Esmail); Data curation, B.A.F.E, Dustin Isleifson (D.I) and S.K (Slawomir Koziel); Formal analysis, B.A.F.E; Funding acquisition, S.K; Visualization, B.A.F.E; Writing—original draft, B.A.F.E; Writing—review and editing, D.I and S.K; Sofware and Resources, B.A.F.E, and S.K; Supervision, D.I and S.K.

Competing interests

The authors declare no competing interests.

Additional information

Correspondence and requests for materials should be addressed to S.K.